Bi-directional Alfvén Cyclotron Instabilities in Spherical Tokamak MAST

S.E. Sharapov, M.K.Lilley[1], R.Akers, N. Ben Ayed, M.Cecconello[2], J.Cook[3], G.Cunningham, E.Verwichte[3] and the MAST Team[a]

CCFE, Culham Science Centre, Abingdon OX14 3DB, UK
[1]Physics Department, Imperial College, London, SW7 2AZ, UK
[2]Dept. Physics & Astronomy, Uppsala University., Uppsala, Sweden
[3] University of Warwick, Coventry, UK

[a] See the Appendix of H.Meyer et al., *Proc. 20th IAEA Fusion Energy Conference 2012 (San-Diego, 2012)* (Vienna: IAEA)

e-mail contact of main author: Sergei.Sharapov@ccfe.ac.uk

Alfvén cyclotron instabilities excited by velocity gradients of energetic beam ions were investigated in MAST experiments with super-Alfvénic NBI over a wide range of toroidal magnetic fields from ~0.34 T to ~0.585 T. In MAST discharges with high magnetic field, a discrete spectrum of modes in the sub-cyclotron frequency range is excited toroidally propagating counter to the beam and plasma current (toroidal mode numbers $n < 0$). At lower magnetic field $\leq$ 0.45 T, a discrete spectrum of Compressional Alfvén Eigenmodes (CAEs) with $n > 0$ arises, in addition to the modes with $n < 0$. At lowest magnetic fields, the CAEs with $n > 0$ become dominant, they are observed in frequency range from ~250 kHz for $n = 1$ to ~3.5 MHz for $n = 15$, well above the on-axis ion cyclotron frequency (~2.5 MHz). The data is interpreted in terms of normal and anomalous Doppler resonances modified by magnetic drift terms due to inhomogeneity and curvature of the magnetic field. A Hall MHD model is applied for computing the eigenfrequencies and the spatial mode structure of CAEs and a satisfactory agreement with the experimental frequencies is found.

1. Introduction

Energetic particles may excite Alfvénic instabilities due to the sources of free energy caused by: 1) radial gradient of the energetic (beam) particle pressure, $\nabla p_b \neq 0$, 2) bump-on-tail of the beam distribution function F_b in energy, $\partial F_b / \partial E > 0$, and 3) temperature anisotropy of the beam, $\partial F_b / \partial v_\perp^2 \neq \partial F_b / \partial v_\parallel^2$, where $v_\perp$, $v_\parallel$ are velocity components perpendicular and parallel to the magnetic field [1]. The instabilities driven by ∇p_b, such as Toroidal Alfvén Eigenmodes (TAE) and fishbones, cause a radial re-distribution/ loss of energetic ions, while the instabilities driven by the velocity gradients may cause a beam energy loss and pitch-angle scattering of the beam ions higher than the classical Coulomb collisions. Instabilities in the ion-cyclotron range of frequency driven by cyclotron resonance interaction with energetic ions has been long recognised as an important channel of releasing the free energy sources due to the velocity gradients [1, 2], and a first theory of weakly-damped eigenmodes in the ion-cyclotron frequency range in realistic plasma configurations has been developed [3, 4].

Ion Cyclotron Emission [5] observed in the earliest JET deuterium-tritium (DT) plasmas has set up a solid stage for a systematic experimental study of the velocity gradient-driven cyclotron instabilities on tokamaks [6, 7]. On JET, the ICE phenomenon was interpreted as a cyclotron instability of compressional Alfvén (also called fast Alfvén or magneto-acoustic waves) eigenmodes (CAEs) excited at alpha-particle harmonics, $\omega \cong l\omega_{B\alpha}$, by centrally born, marginally trapped alpha-particles undergoing drift excursions to the plasma edge where CAEs are localised. Here $\omega_{B\alpha}$ is the cyclotron frequency of alpha-particles and l is an integer number. Since only highly energetic trapped alpha-particles have orbits large enough to reach the edge plasma region, the velocity distribution of the alpha particles in the CAE region has a local bump-on tail, $\partial F_\alpha / \partial E > 0$, at a certain speed and pitch angle. A comprehensive theory of ICE has been developed (see, e.g. [8,9]) convincingly interpreting the ICE data. In particular, the experimentally observed fine splitting of the mode frequencies was explained in [10] as a result of the toroidal drift of trapped energetic ions, which modifies the resonance as $\omega \cong l\omega_{B\alpha} \pm mV_{D\alpha}/r$, where $V_{D\alpha}$ is the toroidal drift velocity of trapped fast ions, and the poloidal mode number, $m > 0$, and $m < 0$, provide two maxima to the instability growth rate and cause the frequency splitting. During the high fusion power DT campaign on JET, further study of ICE has shown that the intensity of the spectral ICE lines was

proportional to the DT fusion rate thus confirming the alpha-particle drive as the source of CAEs excitation [10]. This observation opens the opportunity for using the ICE measurements as a passive diagnostic of the alpha-particles in burning DT plasmas on ITER.

Development of the Spherical Tokamak (ST) concept and the two new large ST machines built, NSTX [12] and MAST [13] with super-Alfvénic NBI, have significantly expanded the opportunities for experimental studies of energetic particle-driven Alfvén instabilities, including these in the frequency range comparable to ion cyclotron frequency [14, 15]. Discrete spectra of modes with frequencies below ion cyclotron frequency driven by nearly tangentional NBI were first observed on NSTX [14], and later on MAST [15]. These modes were identified as CAEs and Global Alfvén Eigenmodes (GAEs) from the Alfvénic character of their frequency evolution with plasma density and magnetic field, the mode polarisation, and through a comparison with theoretically derived spectra of CAE and GAE in the ST geometry [16, 17]. In contrast to the ICE case associated with edge-localised CAEs, the modes driven by NBI in STs were found to be at mid-radius [15]. Although the free energy source of the instability in NSTX [14] was found to be similar to that of ICE, $\partial F_b / \partial E > 0$, the sub-cyclotron range of the mode frequencies and the dominant component of the beam velocity parallel to the magnetic field, required a Doppler shifted wave-particle resonance (1) to be relevant. Indeed, one of the main features of the beam-driven modes in STs is that, in comparison to the ICE data, the mode frequencies deviate significantly from integer multiples of ion cyclotron frequency. Importance of this for the sub-cyclotron frequency modes can be seen from the resonance condition

$$\omega = k_{\|} v_{\|b} + l\omega_{Bb} + \vec{k}_{\perp}\vec{V}_{Db} , \qquad (1)$$

where $k_{\|} \equiv \vec{k} \cdot \vec{B} / B$ and $\vec{k}_{\perp} = \vec{k} \times \vec{B} / B$ are the wave-vectors parallel and perpendicular to the magnetic field, and

$$\vec{V}_{Db} = \frac{v_{\perp}^2 / 2 + v_{\|}^2}{\omega_{Bb}} \left[\mathbf{b} \times \frac{\nabla B}{B} \right] \qquad (2)$$

is the magnetic drift velocity of the beam ions. Doppler frequency shifts well below $\omega = l\omega_{Bb}$ if $k_{\|} v_{\|b} + \vec{k}_{\perp}\vec{V}_{Db} \approx -l\omega_{Bb}$, and since the nearly tangentional NBI generates beam with $v_{\|b} >> V_{Db}$, the parallel wave-vector becomes an important

parameter determining the Doppler shift. It is easy to see next that when $\left|k_{\parallel}\ v_{\parallel b}\right| / \left|\vec{k}_{\perp}\vec{V}_{Db}\right| >> 1$, the normal Doppler resonance with $l = +1$ gives the frequency range below ion cyclotron frequency if $k_{\parallel}\ v_{\parallel b} < 0$ thus determining the directivity of the wave propagation with respect to the parallel beam velocity.

The directivity of the mode propagation excited in the sub-cyclotron frequency range was studied in detail on MAST [18, 19]. It was found that i) with very rare exceptions, almost all the modes propagate towards the beam and the plasma current, i.e. they have negative toroidal mode number, $n < 0$, and ii) modes with higher frequencies have lower mode numbers $|n|$. It became interesting then to search for some MAST reproducible plasma scenarios, in which the beam would excite waves propagating co-beam and co-current, $k_{\parallel}\ v_{\parallel b} > 0$. Anomalous Doppler resonance for $l = -1$ becomes relevant then,

$$\omega = k_{\parallel}\ v_{\parallel b} - \omega_{Bb} + \vec{k}_{\perp}\vec{V}_{Db}\ , \qquad (3)$$

and the free energy source associated with the beam temperature anisotropy, $T_{\parallel b} > T_{\perp b}$, plays a role [20,1]. Although the resonance (3) is well-known for causing a fan-type (i.e. with a strong pitch-angle scattering) instability of run-away electron beams in tokamaks [21], similar effects for ion beams were not explored in detail yet and are of great interest. However, in order to access this particular resonance in infinite homogeneous plasma (and without the drift term), a threshold with respect to Alfvén velocity V_A of $v_{\parallel b} / V_A \approx 2.6$ should be matched. Although toroidal geometry causing the drift in (3) may soften the requirement, still the best way of approaching the anomalous Doppler resonance driving CAEs is to decrease the equilibrium magnetic field and obtain lowest possible values of Alfvén velocity (at constant beam velocity).

The paper presents results of this low-field experiment on MAST in Section 2. Numerical calculations of eigenmodes using the WHALES Hall-MHD model [21] are presented in Section 3. Section 4 discusses the resonance condition, and Section 5 presents conclusions.

2. Transitions in the spectra of Alfvénic modes at decreasing magnetic field

MAST is a small aspect ratio tokamak with typical major and minor radii of R_0=0.86 m and a = 0.6 m respectively. Looking from above the machine, equilibrium toroidal field is in the clockwise direction, while the inductive plasma current and neutral beam injection (NBI) are in the anti-clockwise direction. The tangency radius of NBI is 0.7 m, and in the experiment deuterium (D) NBI with maximum energy $E_b^{\max} \approx$ 65 keV was injected into D plasma thus generating a D beam distribution function with maximum velocity of $V_b^{\max} \approx 2.5 \cdot 10^6$ m/s. The range of operational parameters used for the experiment discussed here was $B_T \approx 0.34$ - 0.585 T, $I_P^{\max} \approx 600$ kA, $n_e(0) \approx (2\text{-}4) \cdot 10^{19}$ m^{-3}, and $T_e \approx (0.8 - 1)$ keV, and the ratio between beam velocity and Alfvén velocity was varied in the range $V_b^{\max} / V_A = 1.54 - 2.26$. The best CAE data was collected when NBI power of ~2 MW was used, while doubling of NBI power caused a significant activity of energetic particle-driven modes in the TAE and fishbone frequency ranges, which dominated the spectrum of the measured Alfvénic perturbations, with the CAE spectrum having much shorter times of existence at lower amplitudes. During the experiment, MAST discharges were in L-mode most of the time, with some short-time transitions into H-mode. Figure 1 shows toroidal magnetic field B_T, inductive current I_P, and NBI power waveforms in three MAST discharges with three different magnetic fields. For detecting electromagnetic waves, 10 OMAHA coils digitised to 10 MHz sampling rate were used allowing measurements up to 5 MHz to be performed [4]. For determining electron density and electron temperature profiles, Thomson scattering diagnostics was employed with high spatial resolution, and MSE diagnostic was used for measuring the safety factor profiles.

In the experiment, B_T was varied from discharge to discharge in order to cover the whole range of toroidal magnetic fields possible on MAST. As B_T decreased, significant changes were observed in both frequency spectrum and toroidal mode numbers n of the modes with frequencies comparable to the ion cyclotron frequency as Figures 3-5 display.

At high $B_T \approx 0.5$ T, only modes propagating counter-beam, i.e. with $n < 0$ are excited. Figure 3 shows both amplitude and phase magnetic spectrograms of the modes excited. The frequency range of the modes observed lies in the range from ~700 kHz to

~1.4 MHz, while the on-axis cyclotron frequency is $f_{Bi}(0) \equiv \omega_{Bi}(0)/(2\pi) \approx 3.8$ MHz so that $f \equiv \omega/(2\pi) \approx (0.18 \div 0.37) f_{Bi}(0)$ (Fig.3). The phase magnetic spectrogram shows toroidal mode numbers of the modes excited, $n = -5,\ ...,\ -10$.

At somewhat lower magnetic field, $B_T \sim 0.4$ T (MAST discharge #27145), in addition to the modes in the sub-cyclotron frequency range ~700 kHz – 1.2 MHz, another type of discrete spectrum arises in a much higher frequency range, $f \approx$ 1.8 MHz – 2.2 MHz as Figure 4 shows. This frequency range is closer to the on-axis cyclotron frequency of ~3 MHz and is comparable to the ion cyclotron frequency at the outer edge of the plasma, ~1.9 MHz. Zoom of the phase magnetic spectrogram shows that this spectrum has positive toroidal mode numbers $n = 8,\ 9,\ 10$, much wider gaps between the frequencies of the modes with different n's, $f_{n+1} - f_n \approx 220$ kHz, and frequencies of the modes increasing with toroidal mode number. For this machine and plasma parameters, the ratio between the beam velocity and Alfvén velocity was $V_b^{\max}/V_A \approx 2$.

Finally, the MAST comparison discharge #27148 with lowest magnetic field, $B_T \sim$ 0.34 T, was performed exhibiting a massive activity of modes in the range from ~250 kHz to ~3.5 MHz, with toroidal mode numbers $n = 1,\ ...,\ 15$. In this discharge, the modes with $n < 0$ in the sub-cyclotron frequency range ceased to exist, the gaps between the frequencies of the modes with different n's become $f_{n+1} - f_n \approx 250$ kHz and modes with higher n's have higher frequencies. For this discharge, the ratio between the beam velocity and Alfvén velocity was $V_b^{\max}/V_A \approx 2.26$. The modes of the highest frequency range exceed the on-axis cyclotron frequency of ~2.6 MHz, so the modes excited are identified as CAE. The profiles of electron temperature and density measured, e.g. around the time of CAE observation at 100 ms, are shown in Figure 6.

During the experiment, neutron camera was employed measuring the profiles of DD neutrons mostly determined by beam-plasma reactions [22]. Although some significant drops in the DD neutron rates were observed in some of the discharges, no obvious effects of CAEs on the neutron rates were observed.

In the discharge with lowest B_T, the discrete spectrum of CAEs was spread down to the extreme values of $n = 1$ observed briefly at low frequency of ~250 kHz (see Fig.5). A similar $n = 1$ mode has been observed for a more extended time in another MAST discharge #27147 with B_T~0.38 T as Figure 7 shows. In this case, no low-frequency

long-lasting modes or any other significant MHD activity was seen at the time of the mode observation, e.g. ~100 ms. This case was taken for the further modelling of the CAEs presented in next Section.

Finally, CAEs in MAST discharge #27148 seems to exhibit some fine structure of the frequency spectrum. Such fine structure was also seen more clearly in a number of other discharges, e.g. in MAST pulse #30080 shown in Figure 8. The frequency split between the modes with the same toroidal mode numbers, is ~40 kHz, which is much smaller than the frequency separation between CAEs with different n's (about 250 kHz), but higher than Doppler shift caused by the beam-driven toroidal rotation of the plasma, ~ 15 kHz. Such fine splitting may be caused by different poloidal mode numbers, similar to the fine splitting observed in ICE [10], or may result from nonlinear effects in the wave-particle interaction similar to the pitchfork splitting of TAE [23].

3. Modelling the spectra of Compressional Alfvén Eigenmodes with Hall MHD

For modelling Compressional waves, a Hall-MHD approach is employed similar to that developed in [24]. In the model used, the Hall term is incorporated as the modified plasma displacement

$$\vec{\eta} = \vec{\xi} - \frac{i\omega}{\omega_{Bi}} \frac{\vec{\xi} \times \vec{B}_0}{B_0}, \tag{4}$$

where $\vec{\xi} = (c / i\omega B_0)[\delta\vec{E} \times \vec{B}_0]$ is plasma displacement due to the cross-field drift velocity associated with perturbed electric field $\delta\vec{E}$. Subsequently, the induction equation reduces to $\delta\vec{B} = \vec{\nabla} \times [\vec{\eta} \times \vec{B}_0]$. The equations for the plasma displacement perpendicular to $\vec{B}_0$ to be solved, have the form:

$$\eta_\psi = \vec{\eta} \cdot \vec{\nabla}\psi, \tag{5}$$

$$\eta_\Lambda = \vec{\eta} \cdot \frac{[\vec{B}_0 \times \vec{\nabla}\psi]}{B_0^2}, \tag{6}$$

and a right-handed coordinate system $(\nabla\psi,\ \nabla\phi,\ \nabla\vartheta)$ is employed, with toroidal angle ϕ increasing anti-clockwise when viewed from above. In contrast to the model developed in [24], which solved equations for three magnetic field components, now the equations for only two displacement variables are solved.

For obtaining a well-converged spectrum of compressional Alfvén waves with $k_{\|}/|k| < 1$, terms linear in the parallel wave-vector are only kept, and terms $\propto (k_{\|}/|k|)^2$ are omitted. In this way, the problem of the coupling of the compressional Alfvén and shear Alfvén waves is resolved in the model used.

The Compressional Alfvén Eigenmodes could have quite global mode structure comparable to the minor radius, so it is necessary to have a good spatial resolution in the whole poloidal cross-section. A finite element method is used in the radial direction, with a spectral method in poloidal direction, and a single harmonic in the toroidal direction. The solution of the Hall MHD equations is searched for as a sum of hybrid Fourier and finite elements

$$\eta_j = \sum_{l=1}^{L} \sum_{m=M_{\min}}^{M_{\max}} c_{l,m} \Lambda_l(\psi) e^{im\vartheta} e^{in\phi}, \qquad (7)$$

where $\Lambda_l(\psi)$ is the l^{th} element in the ψ direction, and $c_{l,m}$ is the complex amplitude of the hybrid element of the displacement. A large number of poloidal harmonics and 5th order b-splines are used as the conforming finite elements for both variables (2), (3) when the Hall term is large. If the Hall term is small, the variable η_ψ is represented with 5th order b-splines, and η_Λ - with 4th order b-splines. In solving the Hall MHD equations no assumption is made on the Hermiticity of the system so the linearly stable Hall-MHD modes get non-zero imaginary components.

For the Hall-MHD modelling, experimental data was taken from MAST discharge #27147 at $t = 100$ ms. At that time, CAE modes were excited with toroidal mode numbers from $n = 1$ to $n = 15$ as Figure 6 shows. Figure 9 shows the safety factor profiles (at $Z = 0$) used in the modelling. Several eigenmodes with somewhat different mode structure and eigenfrequency were computed for every toroidal mode number, with typical well-converged solutions for $n = 1$ and $n = 10$ shown in Figures 10 and 11. Frequency separation between the modes was found to be close to 40 kHz poissibly explaining the experimentally observed fine structure of the CAE spectrum. Figure 12 summarises the modelling results and shows that a good agreement is found in the comparison between the Hall-MHD modelling with the WHALES code and the experimentally observed frequencies.

4. Effects of the magnetic field inhomogeneity and curvature on the cyclotron resonances

Magnetic drift of energetic trapped ions was shown to play an important role in theory of ICE [10], and one can expect that such effect cannot be neglected for the case of passing beam ions. Indeed, considering the resonance condition (3) at decreasing magnetic fields, one notes that the magnetic drift term $V_{Db} \propto 1/\omega_{Bb}$ increases while the cyclotron frequency term itself decreases. Theory considering the case of passing ion drifts in cyclotron instabilities has been developed in [25]. It was shown there in a simple case of axisymmetric tokamak with circular cross-section that the drift velocity term for passing fast ions gives a modified cyclotron resonance condition, which in the case of anomalous Doppler resonance can be written as

$$\omega = \left(k_{\|} + \frac{s}{qR} \right) v_{\|b} - \omega_{Bb} \ , \ s\text{ - integer.} \tag{8}$$

The integer value of s results from the poloidal dependencies of cyclotron frequency, $\omega_{Bb} = \omega_{Bb}(0) \cdot (1 - (r/R)\cos\vartheta)$, and the magnetic drift velocity, $V_{Dr} \propto \sin\vartheta$, $V_{D\vartheta} \propto \cos\vartheta$. Although the resonances with non-zero s provide a smaller particle-to-wave power transfer, the very existence of such resonance makes the critical beam velocity condition described in Introduction, less restrictive. Comparing now second and third terms in (8), one obtains

$$s \approx qR\omega_{Bb} / v_{\|b} = q(R/\rho_{\|b}), \tag{9}$$

which gives s as low as 5-6 when $q \approx 1$ is considered as in Fig. 9 and $\rho_{\|b}^{\max} = V_b / \omega_{Bb} \sim 15$ cm is taken at $B_T \sim 0.34$ T. Figure 13 shows schematically the anomalous Doppler resonance condition (8) corresponding to (8) with several s-terms, and Figure 14 shows the relative location of these resonances with respect to the beam distribution function on MAST.

5. Conclusions

Dedicated MAST experiment with decreasing magnetic field at fixed beam energy has shown excitation of bi-directional Alfvén instabilities. At higher fields exceeding

~0.45 T, excitation of eigenmodes with sub-cyclotron frequencies and mostly negative toroidal mode numbers was observed, while at magnetic fields ≤0.45 T eigenmodes with $n > 0$ start to emerge in the frequency range close to, or exceeding ion cyclotron frequency. These modes with $n > 0$ completely dominate the spectrum of the Alfvén cyclotron instabilities at lowest magnetic fields ~0.34 – 0.38 T. A conclusion is drawn that the modes with $n > 0$ are CAEs due to the frequencies of high-*n* modes exceeding ion cyclotron frequency in MAST.

Modelling of the CAEs was performed with the Hall-MHD model and it was found that this model gives a good agreement with the experimentally measured frequencies and, possibly, explains the fine splitting of the spectrum observed experimentally.

Interpretation of the transition from dominant $n < 0$ mode excitation to dominant $n > 0$ mode excitation was suggested in terms of the anomalous Doppler resonance, and it was found that magnetic drift terms play a significant role, similarly to the case of normal Doppler resonance considered earlier.

Acknowledgment

The authors thank K.G.McClements for support and encouragement in preparing this paper.

References

[1]H.L. Berk, W. Horton, M.N. Rosenbluth, P.H.Rutherford., Nucl. Fusion **15**, 819 (1975).

[2]L.P.Mai, W.Horton, Phys. Fluids **19**, 1242 (1976).

[3]S.M.Mahajan, D.W.Ross, Phys. Fluids **26**, 2561 (1983).

[4]B.Coppi, S.Cowley, R.Kulsrud, P.Detragiache, F.Pegoraro, Phys. Fluids **29**, 4060 (1986).

[5]G.A.Cottrell et al., Nucl. Fusion **33**, 1365 (1993).

[6]S.Cauffman, R.Majeski, K.G.McClements, R.O.Dendy, Nucl. Fusion **35**, 1597 (1995).

[7]O.Da Costa, H.Kimura, S.Moriyama, K.Tobita, and the JT-60 Team, *in Proceed. 5th IAEA TCM on Alpha Particles in Fusion Research, JET Joint Undertaking, Abingdon, UK, 8-11 September 1997, p.37.*

[8]N.N.Gorelenov and C.Z.Cheng, Phys. Plasmas **2**, 1961 (1995).

[9]T.Fulop, Ya.I.Kolesnichenko, M.Lisak, D.Anderson, Nucl. Fusion **37**, 1281 (1997).

[10]Ya.I.Kolesnichenko, T.Fulop, M.Lisak, D.Anderson, Nucl. Fusion **38**, 1871 (1998).

[11]K.G.McClements, C.Hunt, R.O.Dendy, G.A.Cottrell, Phys. Rev. Lett. **82**, 2099 (1999).

[12]D.Gates et al., Phys. Plasmas **10**, 1659 (2003).

[13]A.Sykes et al., Nucl. Fusion **41**, 1423 (2001)

[14]E.D.Fredrickson, N.N.Gorelenkov, C.Z.Cheng, R.Bell, D.Darrow, D.Johnson, S.Kaye, B.LeBlanc, J.Menard, S.Kubota, W.Peebles, Phys. Rev. Lett. **87**, 145001 (2001).

[15]L.C.Appel, T.Fulop, M.J.Hole, H.M.Smith, S.D.Pinches, R.G.I.Vann, and the MAST Team, Plasma Phys. Control. Fusion **50**, 115011 (2008).

[16]N.N.Gorelenkov, E.D.Fredrickson, E.Belova, C.Z.Cheng, D.Gates, S.Kaye, and R.White, Nucl. Fusion **43**, 228 (2003).

[17]H.Smith, T.Fulop, M.Lisak, and D.Anderson, Phys. Plasmas **10**, 1437 (2003).

[18]M.P.Gryaznevich, S.E.Sharapov, M.K.Lilley, S.D.Pinches, A.Field, D.Howell, D.Keeling, R.Martin, H.Meyer, H.Smith, R.Vann, P.Denner, E.Verwichte, and the MAST Team, Nucl. Fusion **48**, 084003 (2008).

[19]M.K.Lilley, *Resonant Interaction of Fast Particles with Alfvén Waves in Spherical Tokamaks*, PhD Thesis, Imperial college, London (2009).

[20]R.Z.Sagdeev, V.D.Shafranov, Sov. Phys. JETP **12**, 130 (1961).

[21]V.V.Parail, O.P.Pogutse, Nucl. Fusion **18**, 303 (1978).

[22]M.Cecconello et al., Nucl. Fusion

[23] A.Fasoli, B.N.Breizman, D.Borba, et al., Phys. Rev. Lett. **81**, 5564 (1998).

[24]H.M.Smith, E.Verwichte, Plasma Phys. Control. Fusion **51**, 075001 (2009).

[25]T.D.Kaladze, A.B.Mikhailovskii, Sov. J. Plasma Phys. **1**, 128 (1975).

Figure captions

Fig.1. Time traces of vacuum equilibrium magnetic field, plasma current, NBI power waveform, on-axis electron density and electron temperature in MAST discharges #27143 (highest B_T), #27145, and #27148 (lowest B_T).

Fig.2. Zoom showing $B_T(0)$ temporal evolution in the comparison discharges shown in Figure 1.

Fig.3. Top: Magnetic spectrograms showing amplitude of δB perturbations excited in sub-cyclotron frequency range in MAST discharge #27143 with high magnetic field $B_T \approx 0.5$ T; Bottom: Phase magnetic spectrogram showing toroidal mode numbers of the modes excited.

Fig.4. (top) Magnetic spectrograms showing amplitude of δB perturbations excited in MAST discharge #27145 with magnetic field $B_T \approx 0.4$ T; (bottom) Zoom of the phase magnetic spectrogram showing toroidal mode numbers of the higher frequency modes.

Fig.5. (top) Magnetic spectrograms showing amplitude of δB perturbations excited in MAST discharge #27148 with magnetic field $B_T \approx 0.34$ T; (bottom) Phase magnetic spectrogram showing toroidal mode numbers of the modes excited.

Fig.6. Electron density and electron temperature profiles measured with high spatial resolution by Thomson scattering diagnostics. Top: $n_e(R)$-profile; middle: $T_e(R)$-profile, and bottom: time slices when the measurements were taken.

Fig.7. (top) Magnetic spectrograms showing amplitude of δB perturbations excited in frequency range ~250 kHz – 3.5 MHz in MAST discharge #27147 with magnetic field $B_T \approx 0.34$ T; (bottom) The phase magnetic spectrogram showing positive toroidal mode numbers of the modes, $n = 1,\ 9,\ 15$.

Fig.8. Top: CAEs observed in MAST discharge #30080 (B_T=0.37 T, E_b=69 keV). Bottom: Zoom showing toroidal mode numbers for all modes with fine splitting of the frequency.

Fig.9. Safety factor profile reconstructed with the use of MSE for MAST discharge # 27147 at t=100 ms.

Fig.10. The WHALES modelling showing eigenfrequency and the mode structure (variables η_ψ and η_Λ) for the $n=1$ CAE in MAST discharge # 27147 at t=100 ms.

Fig.11. The WHALES modelling showing eigenfrequency and the mode structure (variables η_ψ and η_Λ) for the $n=1$ CAE in MAST discharge # 27147 at t=100 ms.

Fig.12. Comparison of the CAE eigenfrequencies with $n=1,\ 9,\ 15$ computed with the WHALES code versus the experimental data for CAE in MAST discharge # 27147 at t=100 ms.

Fig.13. Schematic plot of CAW and SAW dispersion relations with superimposed anomalous Doppler resonance modified by the inhomogeneity and curvature of the magnetic field.

Fig.14. Position of the anomalous Doppler resonances modified by the magnetic drift, with respect to beam distribution $F_b\left(v_\perp,\ v_\parallel\right)$ in the low-B_T case (this Figure will be redone for real MAST simulations during the Refereeing time).

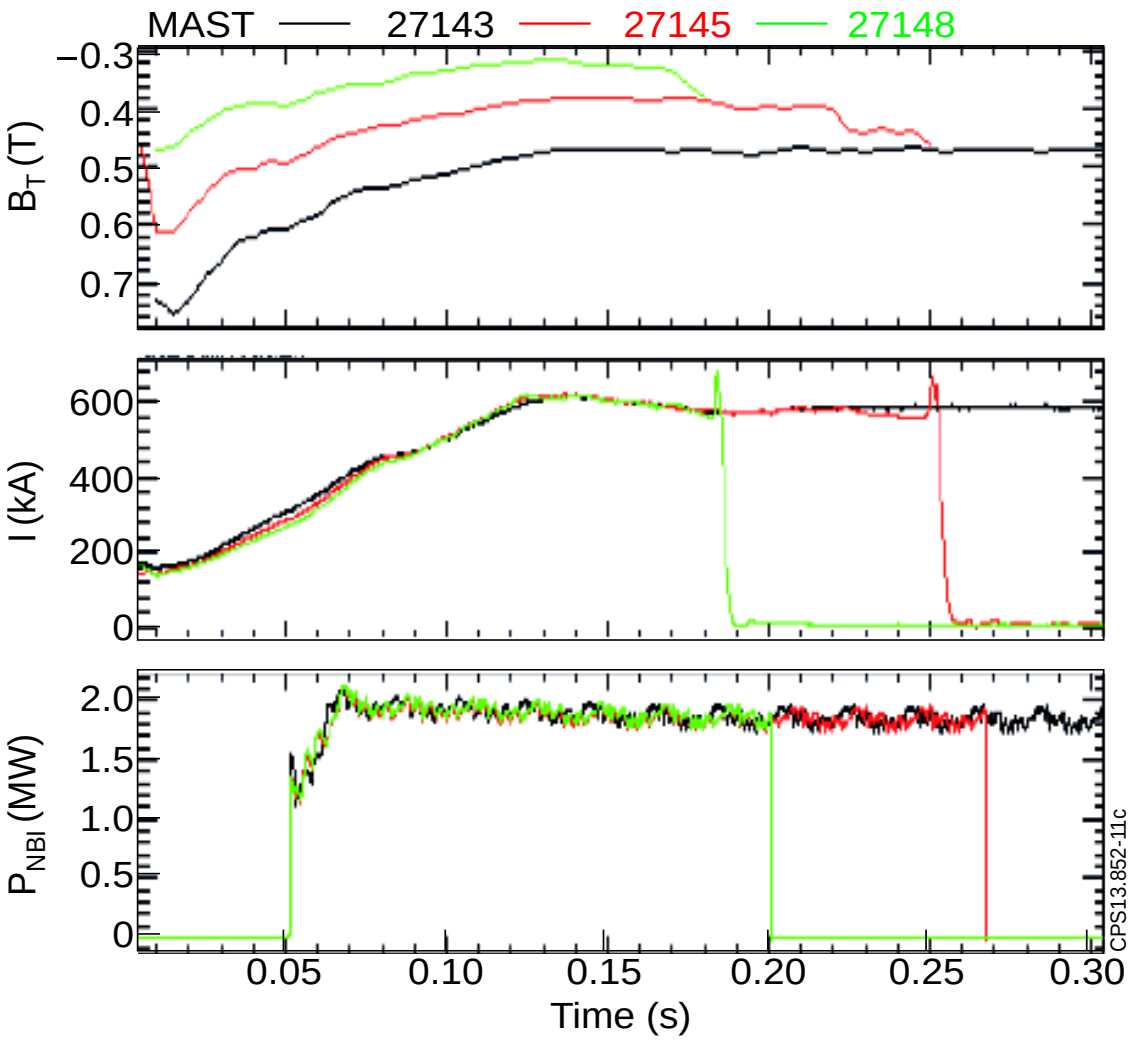
MAST
27143
27145
27148
−0.3
0.4
0.5
0.6
0.7
B_T (T)
600
400
200
0
I (kA)
2.0
1.5
1.0
0.5
0
P_NBI (MW)
0.05
0.10
0.15
0.20
0.25
0.30
Time (s)
CPS13.852-11c

Figure 1.

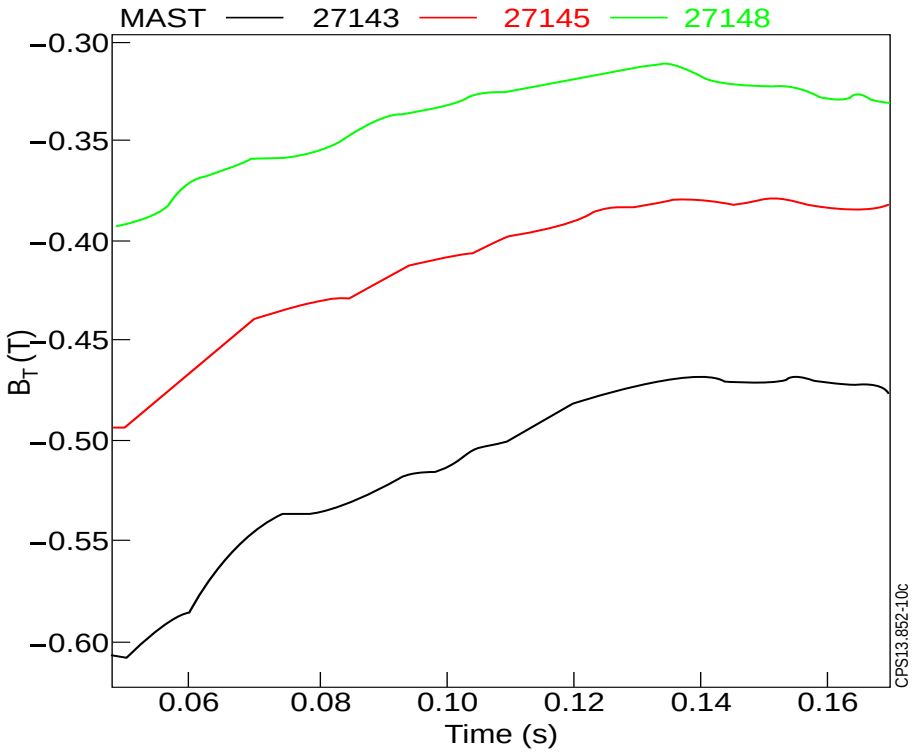
MAST
27143
27145
27148
−0.30
−0.35
−0.40
−0.45
−0.50
−0.55
−0.60
B_T (T)
0.06
0.08
0.10
0.12
0.14
0.16
Time (s)
CPS13.852-10c

Figure 2.

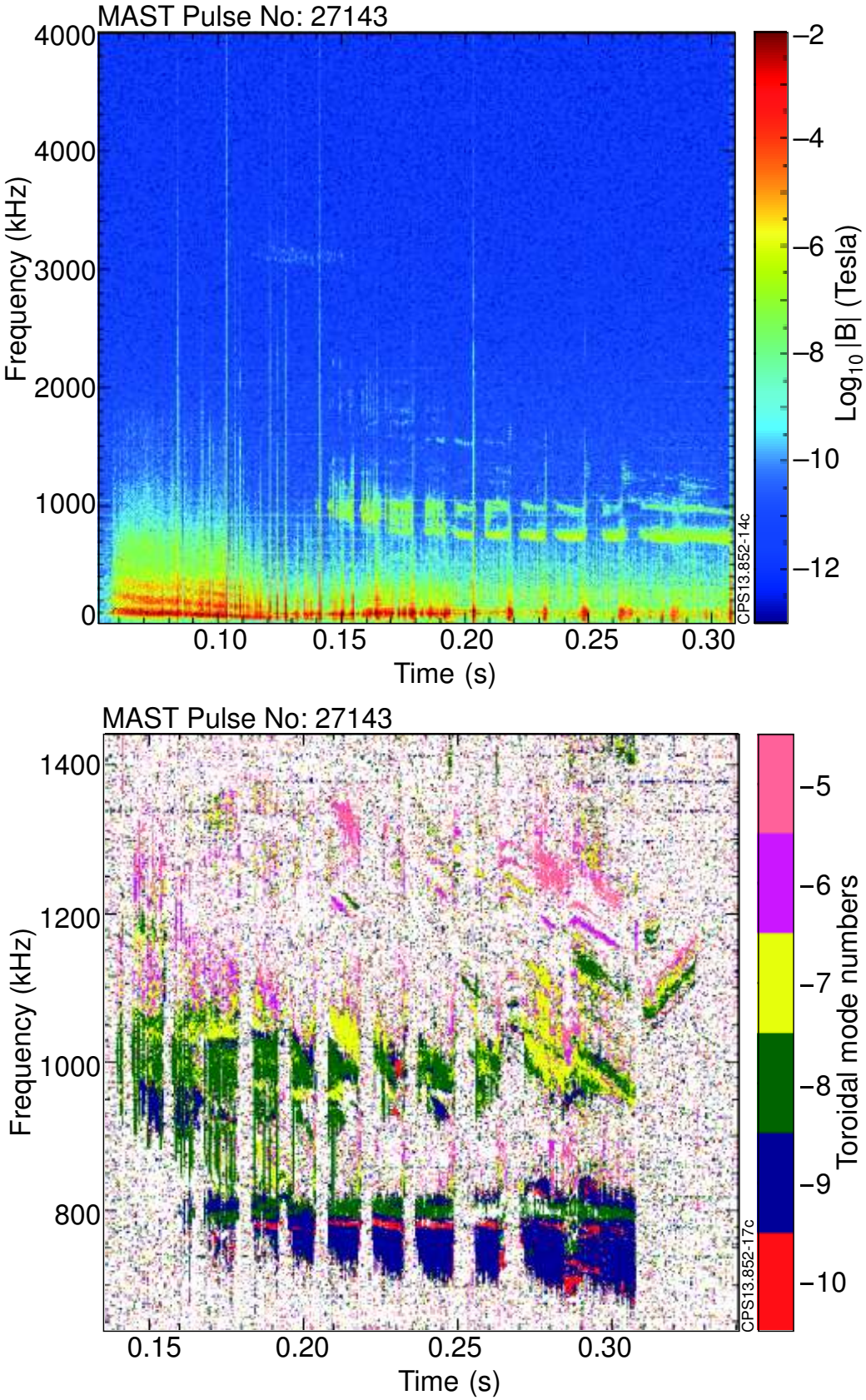
MAST Pulse No: 27143
Frequency (kHz)
4000
4000
3000
2000
1000
0
0.10
0.15
0.20
0.25
0.30
Time (s)
−2
−4
−6
−8
−10
−12
Log10|B| (Tesla)
CPS13.852-14c
MAST Pulse No: 27143
Frequency (kHz)
1400
1200
1000
800
0.15
0.20
0.25
0.30
Time (s)
−5
−6
−7
−8
−9
−10
Toroidal mode numbers
CPS13.852-17c

Figure 3.

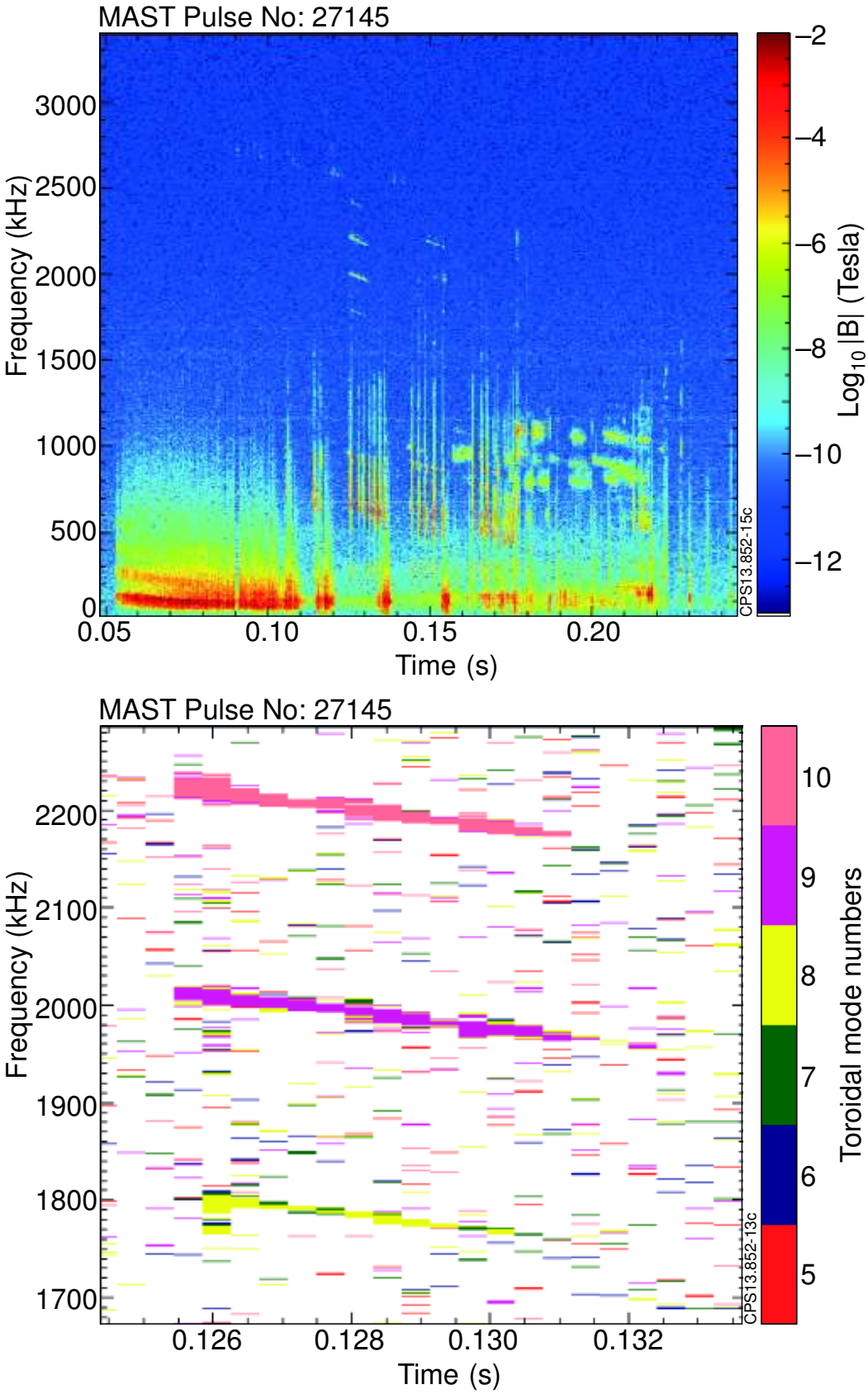
MAST Pulse No: 27145
Frequency (kHz)
3000
2500
2000
1500
1000
500
0
0.05
0.10
0.15
0.20
Time (s)
−2
−4
−6
−8
−10
−12
Log10|B| (Tesla)
CPS13.852-15c
MAST Pulse No: 27145
Frequency (kHz)
2200
2100
2000
1900
1800
1700
0.126
0.128
0.130
0.132
Time (s)
10
9
8
7
6
5
Toroidal mode numbers
CPS13.852-13c

Figure 4.

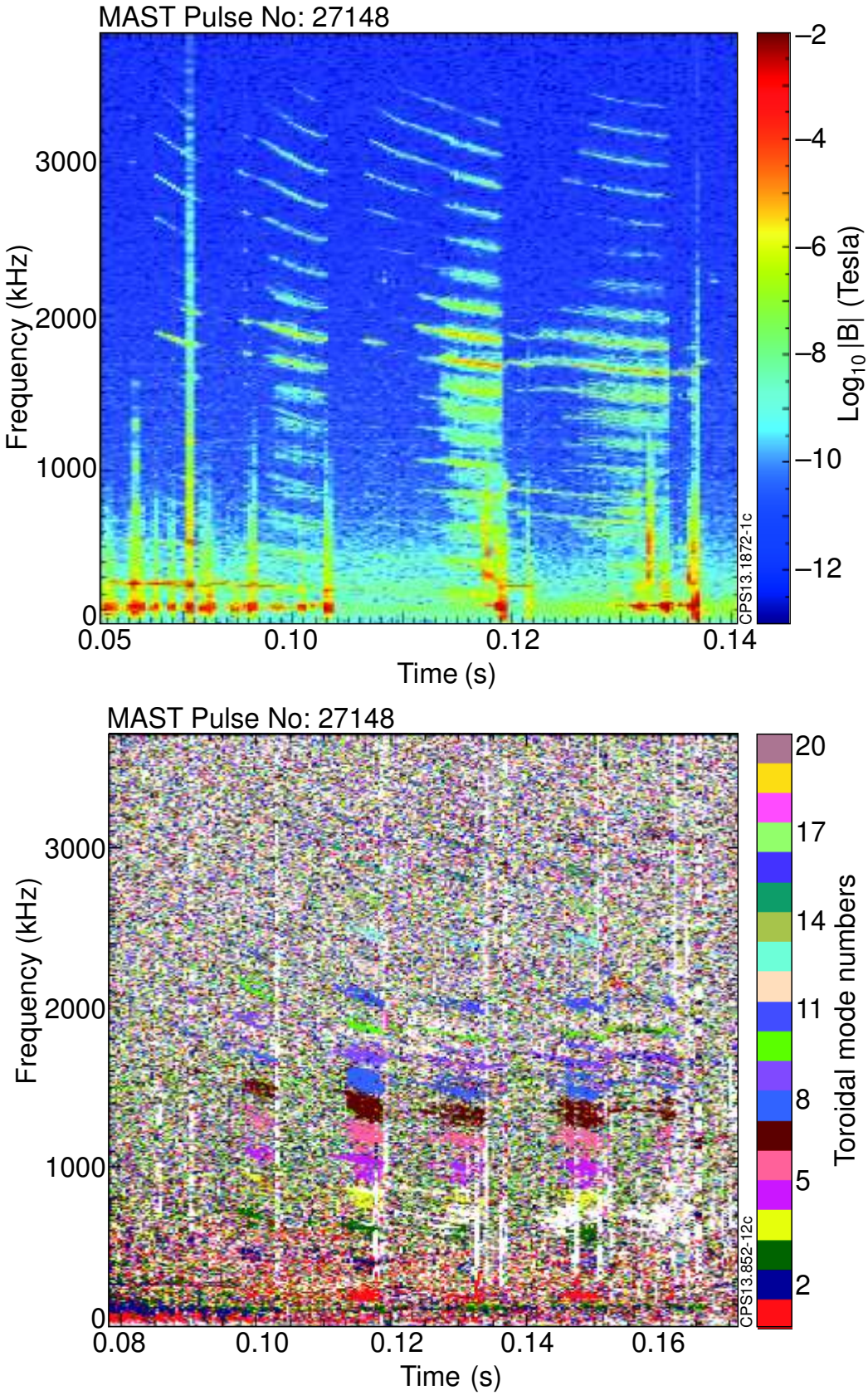
MAST Pulse No: 27148
Frequency (kHz)
3000
2000
1000
0
0.05
0.10
0.12
0.14
Time (s)
−2
−4
−6
−8
−10
−12
Log10|B| (Tesla)
CPS13.1872-1c
MAST Pulse No: 27148
Frequency (kHz)
3000
2000
1000
0
0.08
0.10
0.12
0.14
0.16
Time (s)
20
17
14
11
8
5
2
Toroidal mode numbers
CPS13.852-12c

Figure 5.

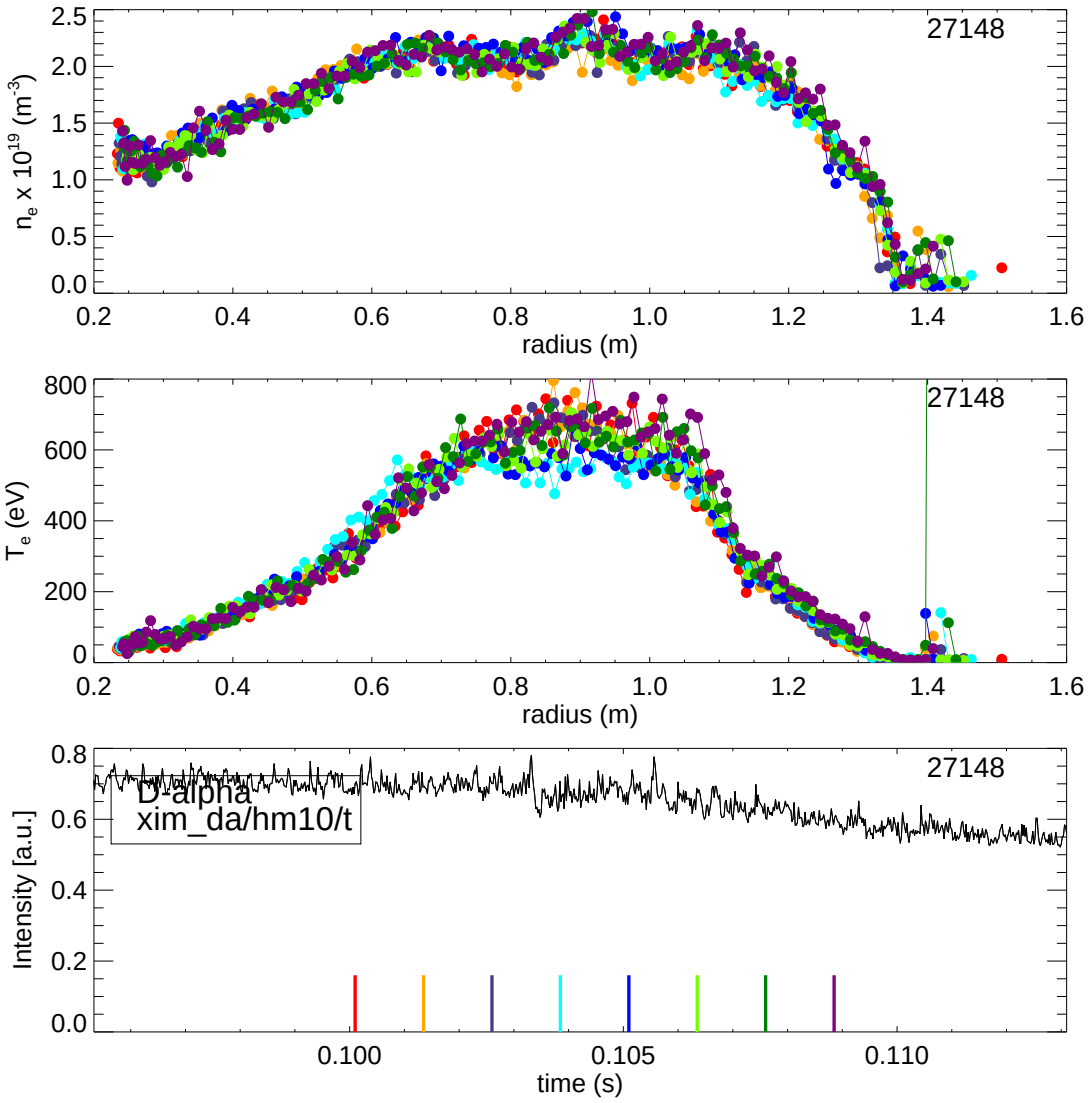
27148
n_e x 10^{19} (m^{-3})
radius (m)
27148
T_e (eV)
radius (m)
27148
D-alpha
xim_da/hm10/t
Intensity [a.u.]
time (s)

Figure 6.

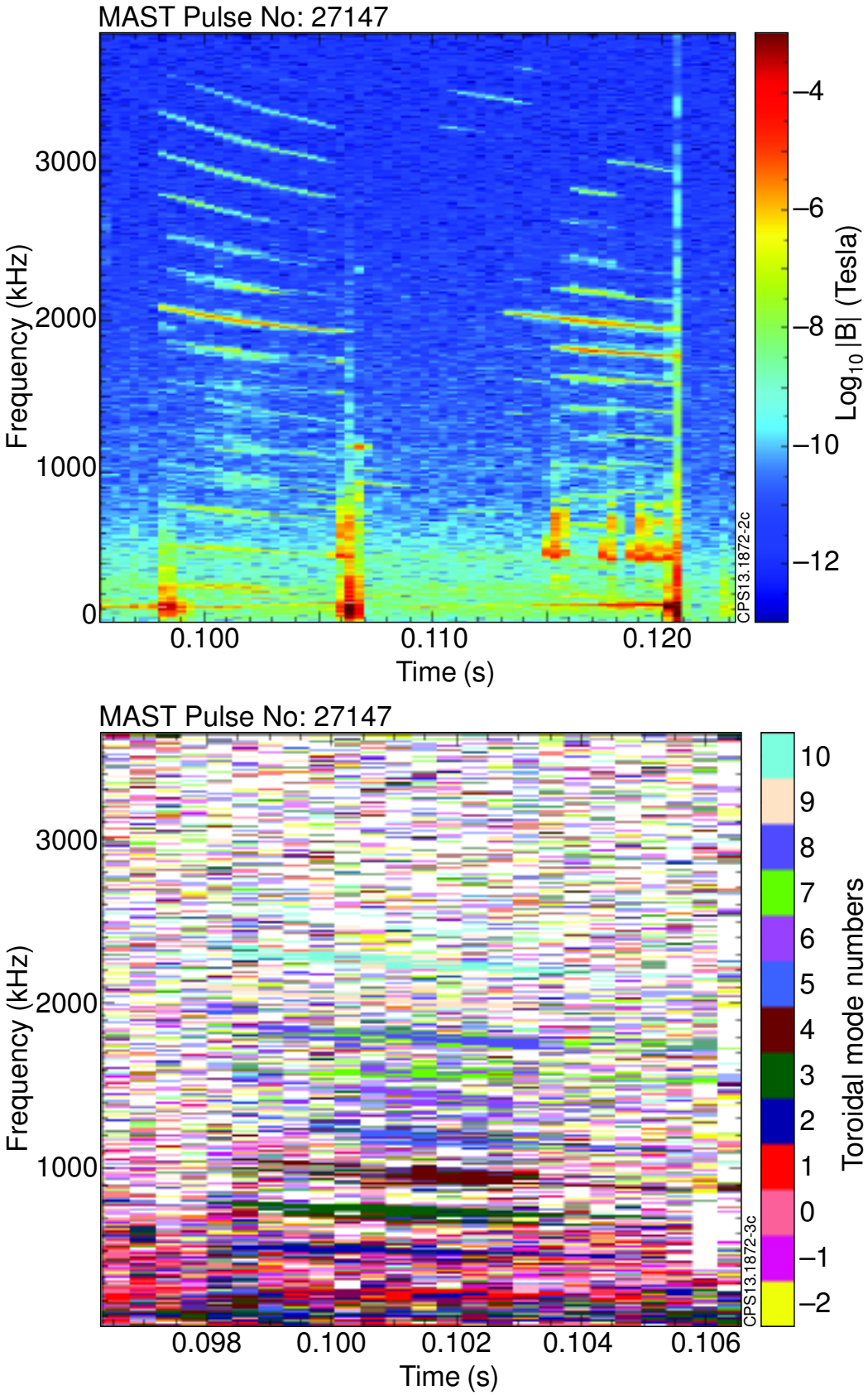
MAST Pulse No: 27147
Frequency (kHz)
3000
2000
1000
0
0.100
0.110
0.120
Time (s)
−4
−6
−8
−10
−12
Log10|B| (Tesla)
CPS13.1872-2c
MAST Pulse No: 27147
Frequency (kHz)
3000
2000
1000
0.098
0.100
0.102
0.104
0.106
Time (s)
10
9
8
7
6
5
4
3
2
1
0
−1
−2
Toroidal mode numbers
CPS13.1872-3c

Figure 7.

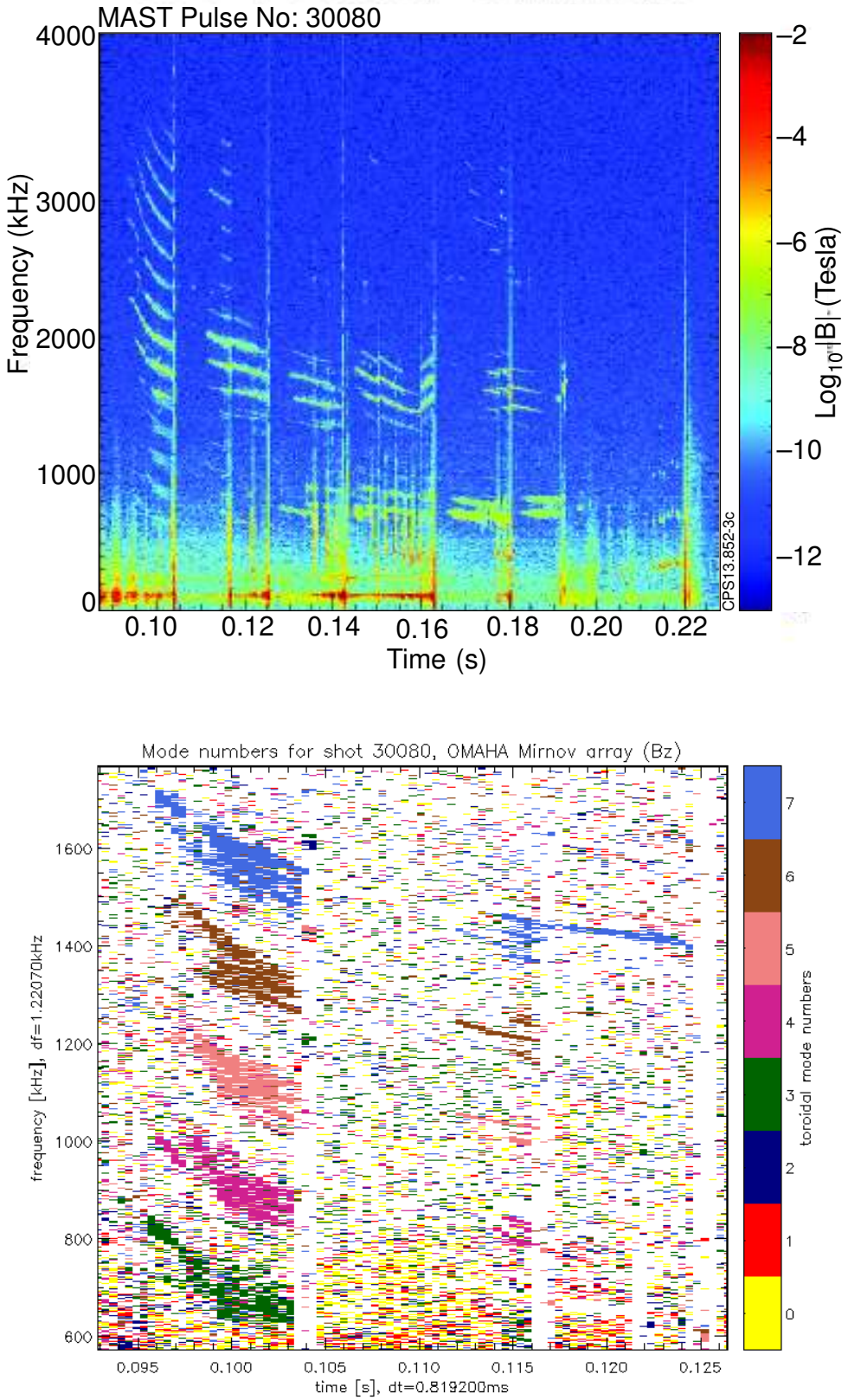
MAST Pulse No: 30080
Frequency (kHz)
4000
3000
2000
1000
0
0.10
0.12
0.14
0.16
0.18
0.20
0.22
Time (s)
CPS13.852-3c
−2
−4
−6
−8
−10
−12
Log10|B| (Tesla)
Mode numbers for shot 30080, OMAHA Mirnov array (Bz)
frequency [kHz], df=1.22070kHz
1600
1400
1200
1000
800
600
0.095
0.100
0.105
0.110
0.115
0.120
0.125
time [s], dt=0.819200ms
toroidal mode numbers
7
6
5
4
3
2
1
0

Figure 8.

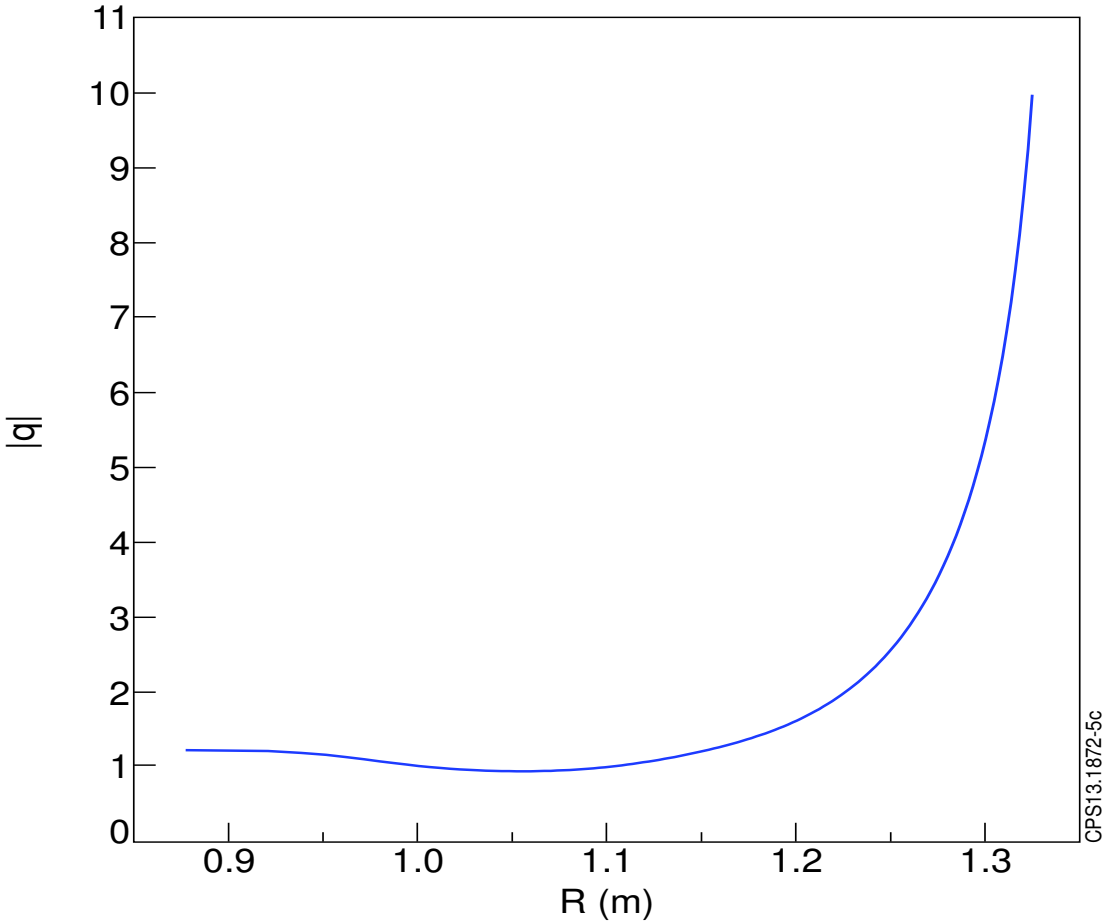

Figure 9.

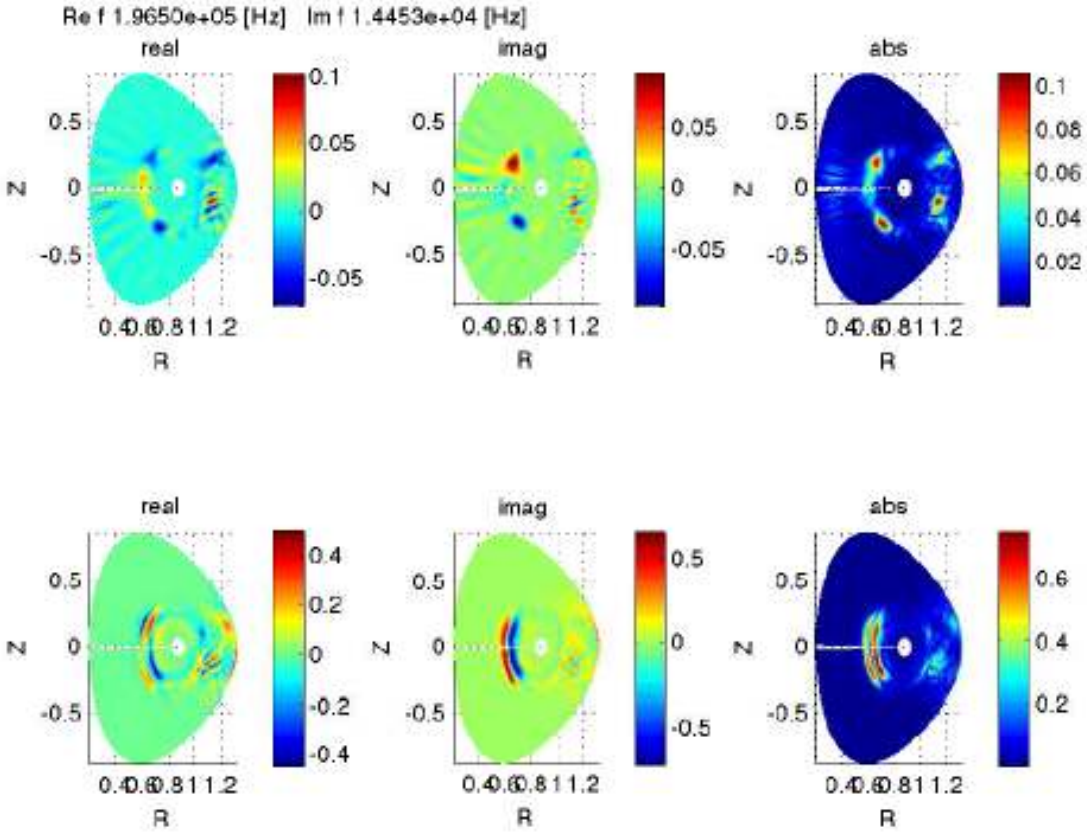
Re f 1.9650e+05 [Hz] Im f 1.4453e+04 [Hz]
real
imag
abs
Z
R
0.5
0
-0.5
0.4 0.6 0.8 1 1.2
0.1
0.05
0
-0.05
0.08
0.06
0.04
0.02
0.4
0.2
-0.2
-0.4

Figure 10.

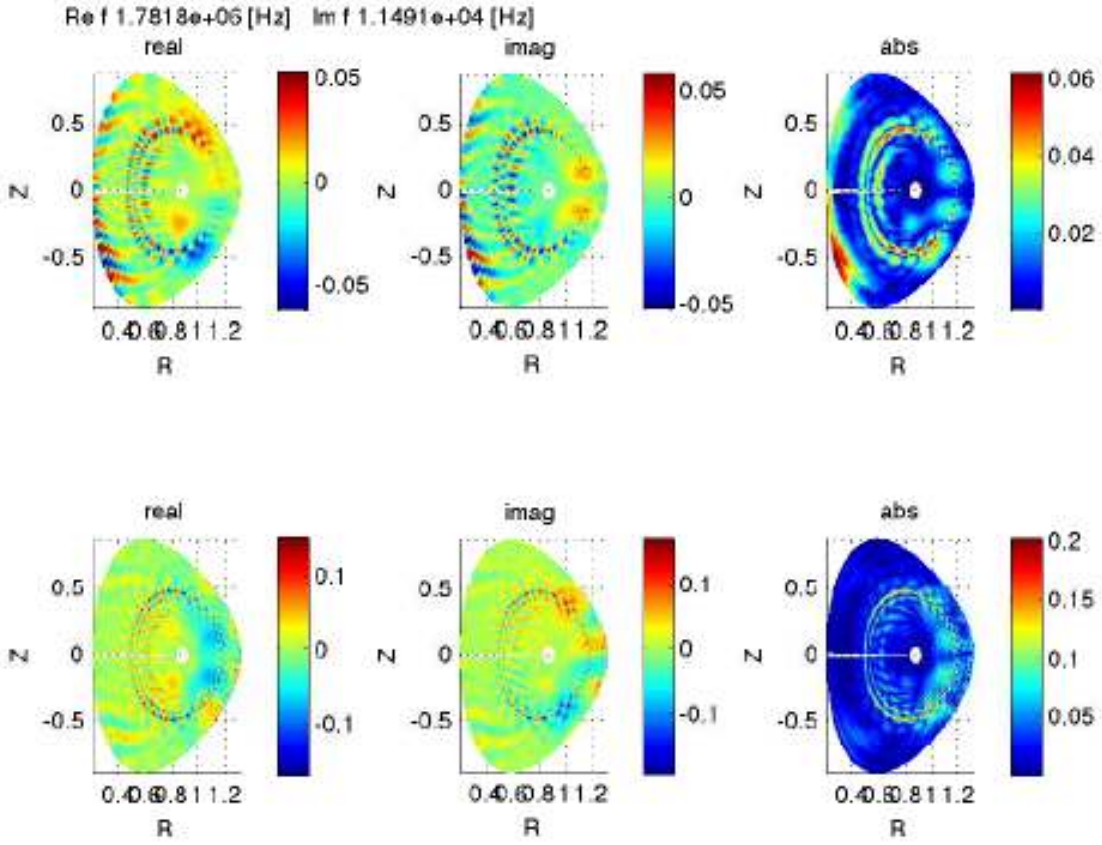
Re f 1.7818e+06 [Hz] Im f 1.1491e+04 [Hz]
real
imag
abs
Z
R
0.5
0
-0.5
0.4 0.6 0.8 1 1.2
0.05
0
-0.05
0.06
0.04
0.02
0.1
-0.1
0.2
0.15

Figure 11.

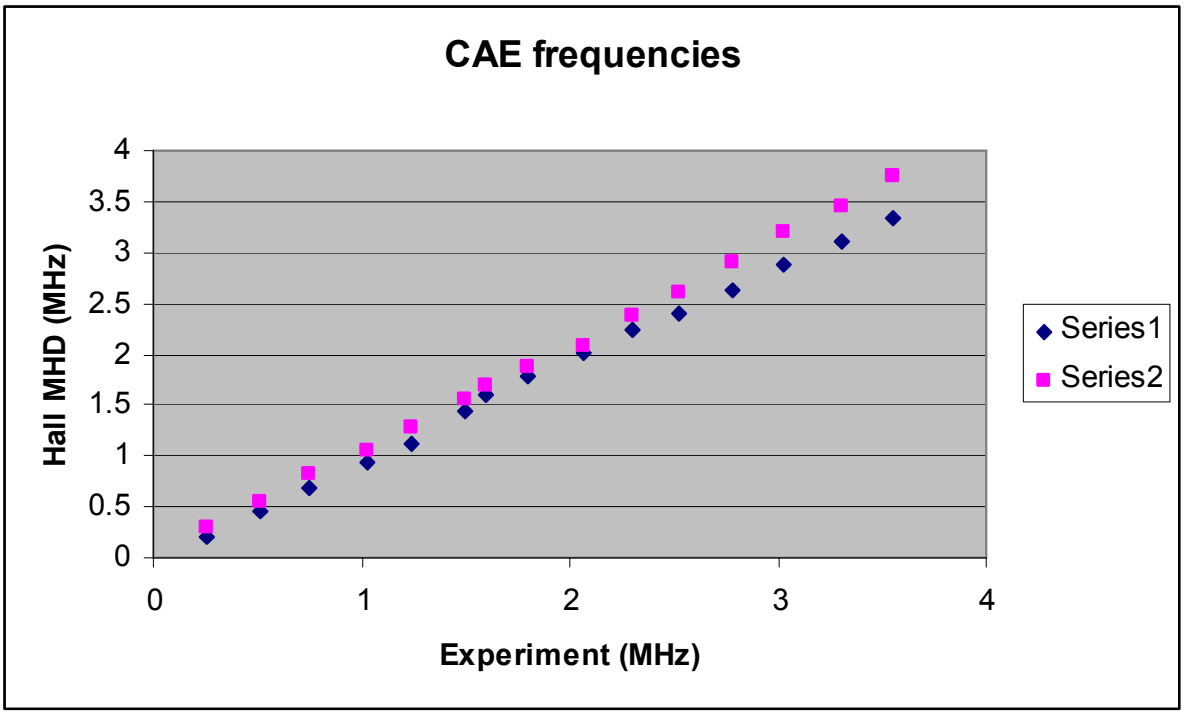
CAE frequencies
Hall MHD (MHz)
Experiment (MHz)
0
0.5
1
1.5
2
2.5
3
3.5
4
0
1
2
3
4
Series1
Series2

Figure 12.

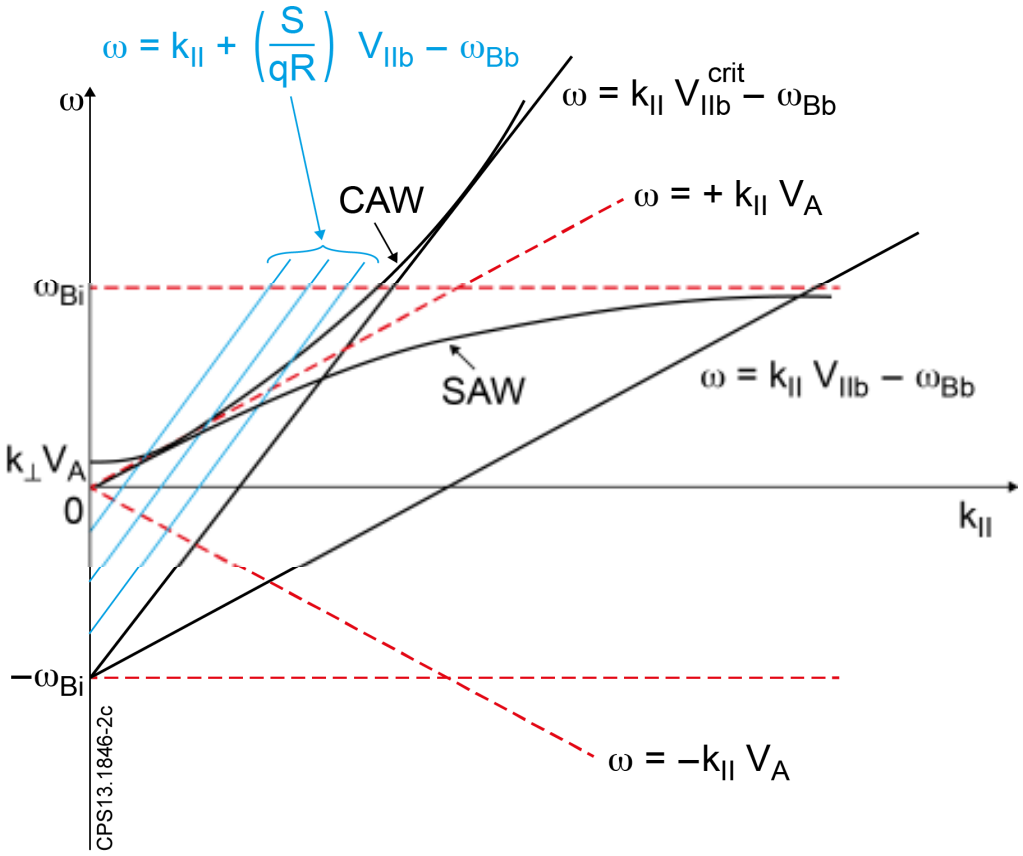
ω = k_II + (S/qR) V_IIb − ω_Bb
ω = k_II V_IIb^crit − ω_Bb
ω = + k_II V_A
CAW
ω
ω_Bi
SAW
ω = k_II V_IIb − ω_Bb
k⊥V_A
0
k_II
−ω_Bi
ω = −k_II V_A
CPS13.1846-2c

Figure 13.

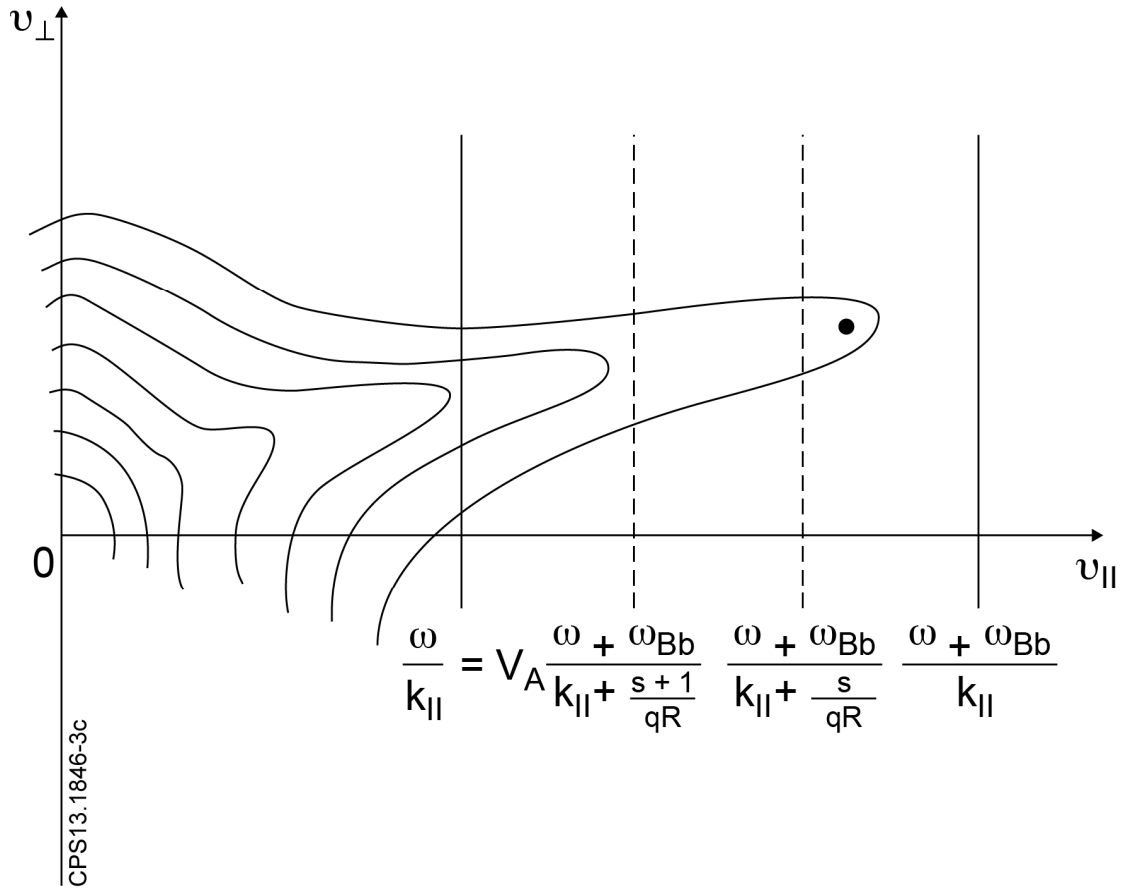
υ⊥
0
υII
ω/kII = VA (ω + ωBb)/(kII + (s + 1)/qR) (ω + ωBb)/(kII + s/qR) (ω + ωBb)/kII
CPS13.1846-3c

Figure 14.